Energy and Buildings 42 (2010) 422–434

Contents lists available at ScienceDirect

Energy and Buildings

journal homepage: www.elsevier.com/locate/enbuild

Numerical study of a naturally cross-ventilated building

K.-S. Nikas, N. Nikolopoulos *, A. Nikolopoulos

Tehnological Education Institute of Piraeus, Mechanical Engineering Department, Fluid Mechanics Laboratory, 250 Thivon & P. Ralli str., Aigaleo 12244, Greece

ARTICLE INFO

Article history:
Received 16 July 2009
Received in revised form 23 September 2009
Accepted 4 October 2009

Keywords:
Numerical simulation
Natural cross-natural ventilation
Building
Air-change rate

ABSTRACT

This paper deals with the numerical three-dimensional prediction of the induced flow patterns around and inside a building, which is cross-ventilated in a natural way. The air change rate is controlled by two opposite openings on the building envelope, as a function of wind velocity and its incidence angle. The numerical methodology is based on the finite volume numerical solution of the Navier–Stokes equations, using the CFD commercial code FLUENT. The numerical results are compared with available experimental data regarding the refresh rate of the building's room and the relative velocity profiles at the window openings, indicating a good agreement. Furthermore, a detailed description of the natural ventilation process is provided, whilst additional information regarding the induced velocity and pressure field is presented; information which cannot be easily extrapolated by experimental methodologies. Finally, the impact of the inner topology of the building on the induced flow field is investigated.

1. Introduction

Nowadays, most of the buildings are ventilated with mechanical systems, despite the increased awareness regarding the cost and environmental impacts of energy use. In this context, the energy consumption related to the operation of heating, ventilation and air-conditioning systems (HVAC) is considerable, since according to recent studies, nearly 70% of the total energy consumption in service and residential buildings can be attributed to HVAC systems [1]. On the other hand, natural ventilation replaces indoor air with fresh outdoor air without using mechanical systems. Hence, natural ventilation can save the energy consumed for the building's ventilation, provided that it ensures both acceptable indoor air quality and satisfactory thermal comfort levels. Besides, it is interesting to note that natural ventilation, potentially appearing to be a cost-effective alternative to the respective mechanically driven, has during the last years attracted the interest of numerous building designers.

The correct design of a naturally ventilated building is a challenging task, due to the complexity of the physical mechanisms involved. The air flow through an opening depends on the pressure difference at both sides of the opening, produced by wind or buoyancy forces, as well as, on the resistance opposed to the air flow by the opening itself. At this point, it should be mentioned, that Allocca et al. [2] revealed that under certain circumstances, the wind effect might not be beneficial, as it may reduce the ventilation rate provided by buoyancy forces alone. In the present work, emphasis is given on the pressure differences due to the wind driven flow. Therefore, in order to optimize such a design, it is necessary to both take into account the pressure distribution around and inside a naturally ventilated building and also configures the induced airflow patterns in detail.

Such kind of information can be provided by full-scale measurements such as those done by Katayama et al. [3], Dascalaki et al. [4], Fernandez and Bailey [5], Koinakis [6] and Straw et al. [7]. Another approach is the use of small-scale models in a wind tunnel to simulate natural ventilation, since the mean flow characteristics, such as the mean pressure, can be adequately modeled for a single building [8–11].

An alternative approach, which gains lead during the last few years, is Computational Fluid Dynamics (CFD), based on the numerical solution of the mathematical equations governing the complex evolved physical mechanisms. The application of such methodologies has become very popular due to the upgrade of computational resources and the improvement of turbulence models, both allowing for a more detailed description of the induced flow field. Besides, the low cost of applying numerical investigation methods instead of costly experiments is an additional benefit that should also be considered.

Three different CFD methodologies are reported in the literature: Direct Numerical Simulation (DNS), Large Eddy Simulation (LES) and Reynolds Averaged Navier–Stokes (RANS) equations. The DNS approach is difficult to apply for simulating natural ventilation in a building due to very high computer memory requirements, whilst LES, which separates flow motion

* Corresponding author.
E-mail addresses: ksnikas@teipir.gr (K.-S. Nikas), niknik@fluid.mech.ntua.gr (N. Nikolopoulos), aristeidhs@gmail.com (A. Nikolopoulos).

0378-7788/$ – see front matter © 2009 Elsevier B.V. All rights reserved.
doi:10.1016/j.enbuild.2009.10.010

into large and small eddies, has been applied for the numerical prediction of the flow field around a building [12–15]. Jiang et al. [16] applied the LES methodology to wind driven ventilation and predicted the pressure and velocity distribution inside and around a scale cubic building model, obtaining good agreement between the numerical results and the corresponding experimental data. In this work, LES models have also been successfully applied to cross-natural ventilation in a group of apartments [17].

Despite the reliability of the LES, RANS models are less time-consuming, whilst Jiang and Chen [18] compared LES and RANS approximations in wind driven natural ventilation, concluding that RANS might not be appropriate for the determination of the ventilation rate. Further comparison between these two approximations may be found in Ref. [19]. On the other hand, Iaccarino and Durbin [20] have successfully used the unsteady version of RANS modeling, in order to study turbulent flows. Recent development of CFD techniques in natural ventilation studies have been applied to simulate both the external flow around buildings and the indoor thermal comfort conditions [21,22]; simulating the combined indoor and outdoor airflow through large openings in wind tunnel models [17]; in a full-scale building placed in a wind tunnel [23] and in full-scale buildings located in a natural environment [24]. Furthermore, Evola and Popov [25] compared the numerical results produced by the standard k–ε and its RNG modification, which predicts better results, for the case of Jiang et al. [16] geometry.

The present investigation is focused on the application of a three-dimensional RANS modeling on wind driven natural ventilation in buildings. The case of a building envelope inside a tunnel forms the basis of the numerical simulation of this work. The results produced are compared with available experimental data, which have been carried out by Larsen [26,27], regarding the ventilation flow rate of the same building geometrical configuration, for different incidence angles, in a full-scale wind tunnel. Moreover, the effect of the inside-geometry on the ventilation rate and the main characteristics of the induced velocity field will be studied, revealing the importance of both the outdoor conditions and the indoor geometry for the ventilation rate in a natural way.

2. Problem description

Wind driven natural ventilation can be distinguished in two main patterns: namely single-sided ventilation and cross-ventilation. The first one is characterized by an opening on one side of the building, whilst in the second one two openings are located in two opposite sides of the building, providing higher rates of ventilation.

Larsen [26,27] performed an extensive experimental work in both a wind tunnel and the open environment, taking into account the effect of significant parameters, such as the magnitude of wind velocity, the temperature difference, the wind direction, the opening area, the geometry and the position of the opening, the shape of the building, as well as the effect of minor parameters such as the surroundings of the building, the intensity of turbulence in the wind, the fluctuations in pressure at the opening and finally the distribution of wind pressure and air velocity in the opening. In the present study, a case of cross-ventilation is simulated for different wind velocities and incidence angles.

3. Numerical details

The present numerical study examines the case of cross-ventilation for fixed geometry openings, focusing on the effect of wind direction and wind velocity on the ventilation rate. The problem setup is shown in Fig. 1. The dimensions of the building's envelope are 5.56 m × 5.56 m × 3 m, giving a clear volume of 68.95 m^3. Each of the two windows has a height of 0.15 m, a width of

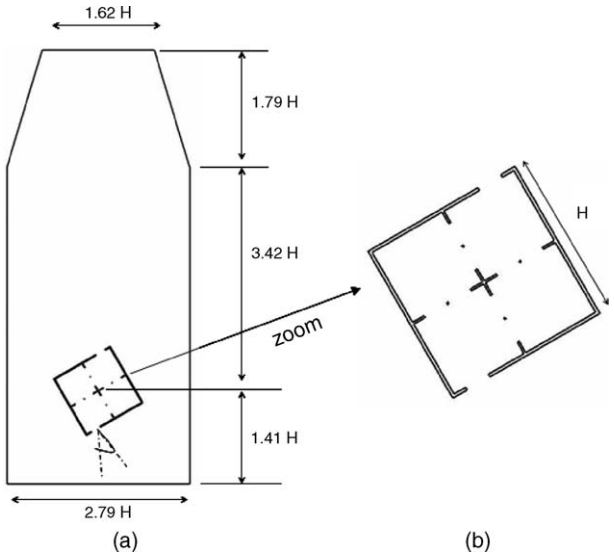

Fig. 1. (a) Dimensions of the ground plan computational domain and (b) ground plan of the building's envelope.

0.86 m and a thickness of 0.1 m, and is located 1.925 m above the ground of the wind tunnel. The computational domain used, displayed in Fig. 2, reproduces the wind tunnel's dimensions, in which the series of experiments was done. The numerical grid used for all cases examined consists of around 3.2×10^6 tetrahedral computational cells, half of which are used in order to discretize the geometry inside the building and 0.8×10^6 cells located at a distance of $H/10$ (H-the building's width) from the building's outer surface. The smallest cell volume is equal to around 2.63×10^{-6} m^3, with an edge of 0.0139 m, and is located within the windows width.

In order to investigate the dependence of the numerical results on the grid resolution, case A_1 was also simulated, giving almost identical numerical results. Note that in case A_1, which will be presented in the following paragraphs, a less fine mesh is used, consisting of 2.3×10^6 tetrahedral computational cells. Further, the maximum difference in the magnitude of total velocity is around 0.78%, indicating that the used numerical grid is dense enough in order to have meshed independent solutions.

4. Numerical methodology

The present numerical methodology is based on the solution of the governing equations [28], which describe the flow field arising from the motion of air around and inside the building, namely the continuity equation for mass transfer as well as the momentum and turbulence-modeling equations. As far as the boundary conditions are concerned, enhanced wall functions are implemented in the wall boundaries of the computational domain. The wall boundary conditions for the k equation in the k–ω models are treated in the same way as the k equation is treated when enhanced wall treatments are used with the k–ε models [28]. This means that all boundary conditions for wall function meshes will correspond to the wall function approach, whilst for the fine meshes, the appropriate low-Reynolds-number boundary conditions are applied. Fluent's algorithm achieves this by blending the linear (laminar) and logarithmic (turbulent) laws of the wall using a function suggested by Kader [29].

A zero first gradient is considered for all variables at the outlet of the computational domain and the velocity's inlet profile is assumed to be uniform, as in the experimental setup. Additionally, computations are performed assuming steady state conditions and incompressible air flow, whilst a second-order discretization

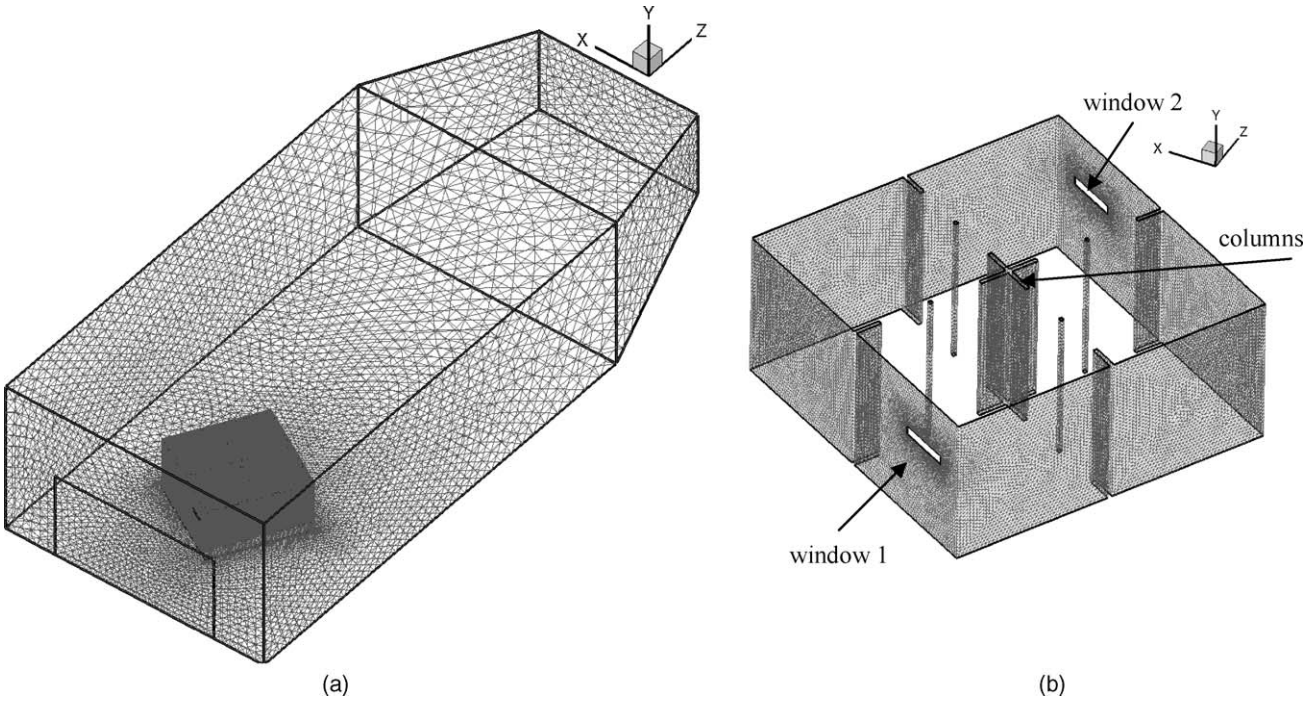

Fig. 2. (a) Computational domain and (b) building's envelope numerical grid.

scheme (QUICK) is used for the spatial terms of the convection source.

In this context, the continuity equation is given by the following expression:

$$\frac{\partial \rho}{\partial t} + \nabla \cdot (\rho \vec{u}) = 0 \tag{1}$$

whilst, the conservation of momentum is described by the following equation:

$$\frac{\partial}{\partial t}(\rho \vec{u}) + \nabla \cdot (\rho \vec{u}\vec{u}) = -\nabla p + \nabla \cdot (\bar{\bar{\tau}}) + \rho \vec{g} + \vec{F} \tag{2}$$

where p is the static pressure, $\bar{\bar{\tau}}$ is the stress tensor, ρg is the gravitational body force and $\vec{F}$ the external body force, which in the present study is equal to zero.

For simulating the flow turbulence, the empirical standard k–ω model, which is based on model transport equations for the turbulence kinetic energy, k, and the specific dissipation rate, ω, is adopted in the present study. As the k–ω model has been modified over the last years, production terms have been added to both the k and ω equations [27], which have improved the accuracy of the model for predicting free shear flows, as follows:

$$\frac{\partial}{\partial t}(\rho k) + \frac{\partial}{\partial x_i}(\rho k u_i) = \frac{\partial}{\partial x_j}\left(\Gamma_k \frac{\partial k}{\partial x_j}\right) + G_k - Y_k + S_k \tag{3}$$

$$\frac{\partial}{\partial t}(\rho \omega) + \frac{\partial}{\partial x_i}(\rho \omega u_i) = \frac{\partial}{\partial x_j}\left(\Gamma_\omega \frac{\partial \omega}{\partial x_j}\right) + G_\omega - Y_\omega + S_\omega \tag{4}$$

where G_k and G_ω represent the generation terms of k and ω, respectively, Γ_k and Γ_ω represent the effective diffusivity of k and ω, whilst Y_k and Y_ω represent the dissipation of k and ω due to turbulence [27].

The effective diffusivities for the k–ω model are given by

$$\Gamma_k = \mu + \frac{\mu_t}{\sigma_k} \tag{5}$$

$$\Gamma_\omega = \mu + \frac{\mu_t}{\sigma_\omega} \tag{6}$$

where σ_k and σ_ω are the turbulent Prandtl numbers for k and ω, respectively, μ is the molecular viscosity whilst the turbulent viscosity, μ_t, is computed by combining k and ω as follows:

$$\mu_t = \frac{\rho k}{\omega} \tag{7}$$

Finally, the generation terms of k and ω are defined as:

$$G_k = -\rho \overline{u_i' u_j'} \frac{\partial u_j}{\partial x_i} \tag{8}$$

$$G_\omega = \frac{\omega}{k} G_k \tag{9}$$

The turbulence intensity, I, is defined as the ratio of the root-mean-square of the velocity fluctuations, u', to the mean flow velocity u_{avg}. For the inlet turbulence intensity a value of equal to 3% is used. The relationship between the turbulent kinetic energy, k, and turbulence intensity, I, is:

$$k = \frac{3}{2}(u_a \cdot I)^2 \tag{10}$$

The respective turbulence dissipation rate is calculated via the following formula, where as a turbulence length scale l, the hydraulic diameter of the inlet boundary is used equal to 6.9 m.

$$\varepsilon = C_\mu^{3/4} \cdot \frac{k^{3/2}}{l} \tag{11}$$

where C_μ is an empirical constant specified in the turbulence model (approximately equal to 0.09).

5. Results and discussion

In order to study and optimize the ventilation performance of a building without using mechanical components, i.e. using natural way ventilation, detailed airflow information around and inside the building is needed. This information includes the velocity and pressure distributions across the entire area of interest, which can then be used to determine the ventilation rate. The following

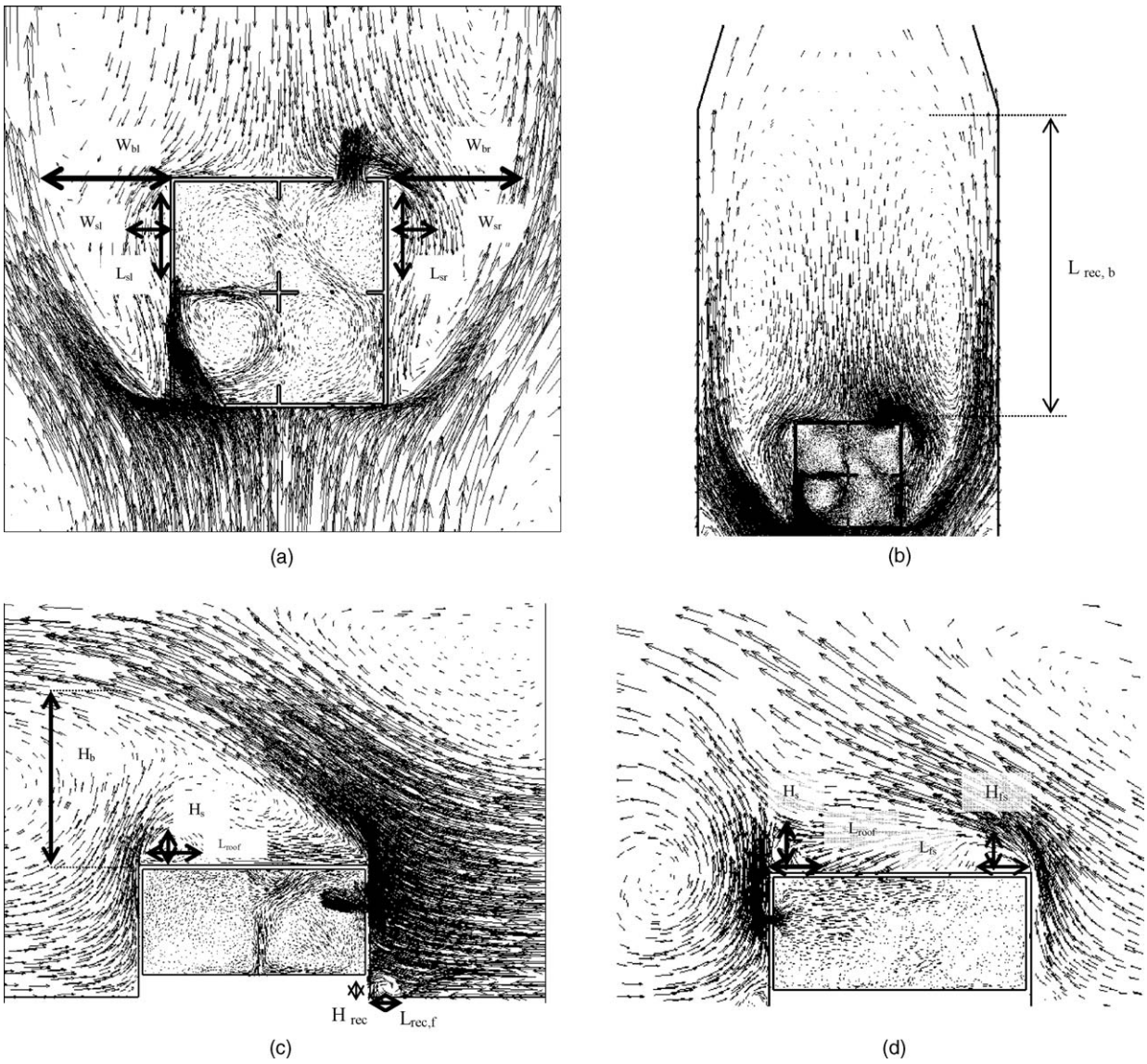

Fig. 3. (a and b) Main dimensions of the induced velocity field at parallel plane $Y = 2$ m, (c) normal to inlet's window and (d) normal to outlet's window.

paragraphs present both numerical and experimental results for 12 different cases, based on the variation of two main parameters. More precisely, the problem main variables include the air free-stream velocity (1, 3 and 5 m/s), configured by the respective Reynolds number (equal to 3.6×10^5, 1.08×10^6 and 1.8×10^6 correspondingly) and the air direction (incidence angle of 0, 30 and 60 and -90°). Finally, it should be mentioned that the Reynolds number is defined as $\mathrm{Re} = U_\infty \cdot H/\nu$ (U_∞ wind free-stream velocity, ν the kinematic viscosity of air at 20 °C), whilst in each case, the predicted induced velocity and pressure field at the areas of interest are presented.

Furthermore, for the better description of the induced pressure field, its dimensionless form is used, which is equal to:

$$C_p = \frac{P - P_{inlet}}{0.5 \cdot \rho \cdot U_\infty^2} \tag{12}$$

5.1. Velocity and pressure distribution

In order to describe the induced velocity and pressure field for all cases, Fig. 3 presents the main characteristics of the flow field for the case of zero incidence angle of the free-stream velocity, with their respective dimensions at different planes. At the horizontal plane passing through the windows, two main recirculation areas of opposite direction are induced on both sides of the building and their widths are defined as W_{bl} and W_{br} (Fig. 3a). Furthermore, behind the building a large recirculation of length defined as $L_{rec,b}$ (Fig. 3b) is induced, which reattaches the left and the right side wall of the building forming smaller recirculation areas with dimensions of W_{sl}, L_{sl} and W_{sr}, L_{sr}, respectively (Fig. 3a). Regarding the normal planes of the building passing from the center of the inlet and outlet openings, again a recirculation zone exists, in which the maximum height is defined as H_b, whilst the recirculating flow reattaches the roof of the building roof inducing a small recirculation to its corner, with dimensions H_s and L_{roof}. Finally, in front of the building close to its bottom a small recirculation area is formed with dimensions $H_{rec,f}$ and $L_{rec,f}$ (Fig. 3c). In cases that a recirculation zone is evident only above the building's roof, as in Fig. 3c, and it has a maximum height equal to H_b. In the case, where above the building's roof both a detachment and a reattachment zone are evident, their dimensions are defined as H_s, L_{roof} and H_{fs} and $L_{f,s}$ respectively as in Fig. 3d.

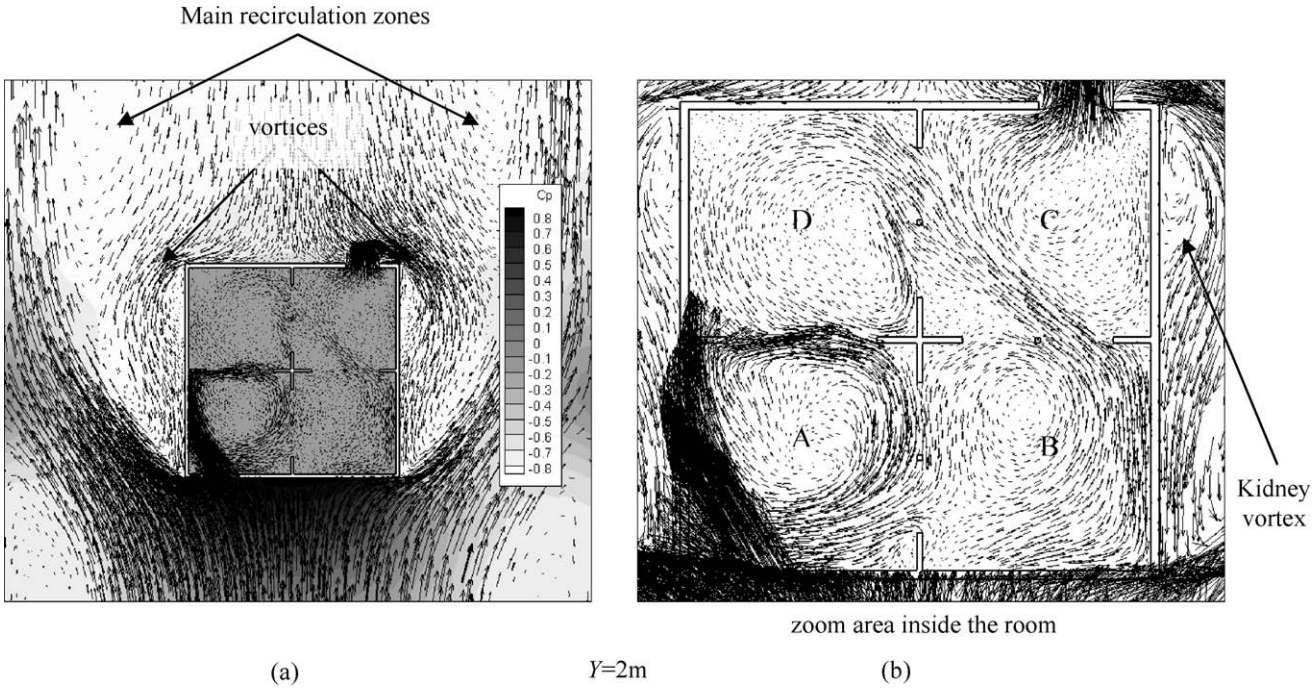

Fig. 4. Induced pressure and velocity field for case A_1.

5.1.1. Incidence angle of 0°: cases A_1 (U_∞ = 1 m/s), A_2 (U_∞ = 3 m/s), A_3 (U_∞ = 5 m/s)

The first cases, used as reference studies in order to compare with the following ones (incidence angle not equal to 0°), are described by an incidence angle of 0° and a wind velocity of 1, 3 and 5 m/s. In this context, Fig. 4a shows the pressure distribution and the induced velocity field at the plane laying in the middle of the openings height, Y = 2 m. The maximum pressure, which acts on the windward face of the building, is equal to 80% of the initial total air inlet kinetic energy for all the three sub-cases.

The most important feature shown outside the building is the formation of two main recirculation areas, covering the whole length of the side walls and a small area of the leeward wall of the building (Fig. 4a). Both of them seem to be equal to their dimensions (Table 1) due to the flow symmetry at 0°. Moreover, these areas include another pair of small vortices, attached at both end-walls of the building, which seem to be of unequal dimensions, due to the fact that the air, flowing out of the leeward opening, drifts into the reattachment zone of the right side vortex, by increasing its length and width by almost 30%. As the wind free-stream velocity increases (cases A_2 and A_3, Table 1), the width and length of the right-side small vortex are increased, caused by the greater mass flowing out of the leeward opening. Furthermore, in the case of the highest air velocity value of 5 m/s (case A_3), a kidney vortex is evident on the right side of the building, as a succession of the small vortex appeared in lower velocity cases.

Inside the building, as Fig. 4b shows, despite the incidence angle of 0° of the air free-stream velocity, the majority of the mass enters the inlet opening with an approximate angle of 20° (*XZ*-plane), due to its simultaneous movement parallel to windward wall after hitting the building and drifting towards the inlet opening.

Moreover, four main vortices at the *XZ*-plane (rooms A, B, C and D respectively), are induced with an opposite direction for sections A and C to sections B and D, whilst they are extended from the ground of the building up to a height equal to approximately 2.75 m, whilst the vorticity's magnitude is predicted to be behind the window inlet in section A of the building. However, the dimensionless vorticity is of the same order for all the cases examined (A_1, A_2 and A_3), revealing the non-dimensional character of the physics governing the mechanisms of natural ventilation of a building. Despite the complexity of the flow field inside the building, and especially at each room, the flow exits the building, by having an almost perpendicular direction to the opening.

Regarding the normal planes inside the building, passing from the inlet and outlet opening centers, in the quarter-section behind the windward window (room A), very intensive vortices exist (Fig. 4b), the strength of which increases as the wind free-stream velocity increases. However, in sections C, B and D not well-formed vortices at the normal planes to the building's roof are observed.

Table 1
Dimensions of induced flow field characteristics for cases A_1 to B_3.

Case	W_{bl}	W_{sl}	L_{sl}	W_{br}	W_{sr}	L_{sr}	H_b (inlet wind)/ (outlet wind)	H_s (inlet wind)/ (outlet wind)	L_{roof} (inlet wind)/ (outlet wind)	$L_{rec,f}$ (inlet wind)/ (outlet wind)	$H_{rec,f}$ (inlet wind)/ (outlet wind)	$L_{rec,b}$	$C_{p,max}$	C_p wind, inlet	C_p wind, out
A_1	3.17	0.56	2.15	3	0.63	2.95	3.53/3.85	0.84/0.92	1.62/1.86	0.86/0.72	0.69/0.64	16.08	80%	0.703	0.34
A_2	3.17	1.44	3.02	3	1.07	3.14	3.61/3.63	2.04/1.13	1.85/1.88	0.8/0.77	0.65/0.71	16.11	80%	0.71	0.38
A_3	3.09	0.7	3.25	3.09	1.15	3.77	3.61/3.43	1.29/1.96	2.08/1.82	0.77/0.83	0.65/0.73	16.55	80%	0.74	0.43
B_1	–	–	–	5.73	–	–	2.76/3.75	0.15/0.57	0.36/1.90	0.69/0.86	0.53/0.66	14.6	100%	0.69	0.31
B_2	–	–	–	5.96	–	–	2.77/3.56	0.13/1.04	0.36/2.49	0.638/0.95	0.51/0.67	13.7	100%	0.68	0.32
B_3	–	–	–	6.05	–	–	2.76/3.51	0.18/1	0.38/3.04	0.55/0.99	0.45/0.7	12.7	100%	0.67	0.36

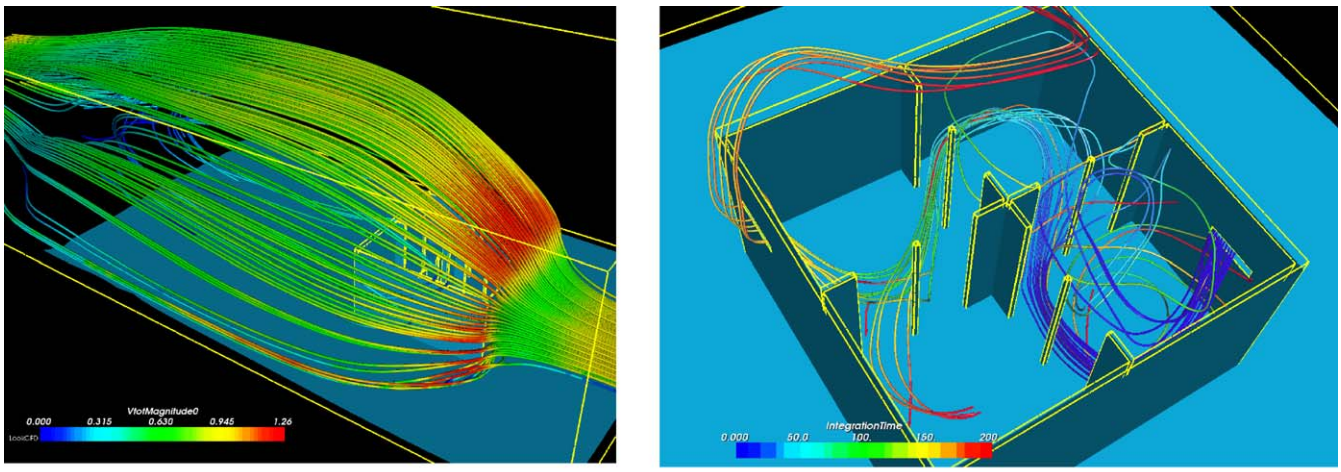

Fig. 5. (a) Flow pathlines around the building and (b) inside the building for case A_1.

Outside and on the top of the building, a big recirculation zone is induced with dimensions given in Table 1, whilst a small vortex is attached to the building's roof at its edge, laying from the side of the leeward window. As far as the dimensions of the vortices above the building's roof are concerned, the maximum height H_s is predicted for case A_2 (Table 1), for the plane passing above the window's inlet, whilst the respective dimension of the vortex attached to the building's roof at the normal plane passing from the middle of the outlet window H_s (outlet window) increases with the Reynolds number (Table 1). The reattachment length of the small vortex for the $X = 5.93$ m plane (L_{roof} (outlet window)) is increasing with increasing Reynolds numbers (cases A_1, A_2 and A_3, Table 1), whilst for plane $X = 9.54$ m it is of almost the same magnitude and equal to around 1.85 m (Table 1).

The main reattachment zone behind the building, $L_{rec,b}$, extends to around 16 m, for all the cases examined (A_1, A_2 and A_3), indicating that it is strongly affected by the building and the wind tunnel geometry, rather than by the wind velocity of this order of magnitude.

As far as the local dimensionless pressure coefficient, C_p, across the inlet ($X = 5.93$ m) and outlet openings ($X = 9.54$ m) levels are concerned, these are equal to 0.7 and 0.35 respectively, and remain the same for all the cases with 0° of incidence angle of wind (A_1, A_2 and A_3). Ideally, these values should have been equal; nevertheless the spatial pressure distribution just outside the outlet window varies significantly, thus making the calculation of C_p at this area difficult.

Fig. 5a and b presents the induced streamlines both around and inside the building for case A_1, coloured with the velocity's magnitude and the integration time of their calculation respectively.

5.1.2. Incidence angle of 30°: cases B_1 ($U_\infty = 1$ m/s), B_2 ($U_\infty = 3$ m/s), B_3 ($U_\infty = 5$ m/s)

The cases described in this section are characterized by the same Reynolds number with the corresponding ones of the previous section, but by a different incidence angle of 30°. Fig. 6a shows the pressure distribution and the induced velocity field at the plane lying in the middle of the openings' height, $Y = 2$ m. The maximum pressure, which acts on the windward face of the building for the cases B_1, B_2 and B_3, compared to the cases A_1, A_2 and A_3 is altered and reaches the limit of 100% of the initial total air inlet kinetic energy.

In contrast to the cases with an incidence angle of 0° the recirculation zone on the left side of the building has disappeared and the air travels almost in parallel and attached to the buildings wall, since it is supported by the incidence angle of 30°. On the contrary, on the right side of the building a large recirculation area is created away from the wall. Moreover, its maximum width W_{br} (Table 1) is slightly increasing with Reynolds number due to the fact that the momentum of the recirculated flow behind the building becomes also higher. In addition, a small reattachment vortex is produced on the right corner of the building and is extended for a length of $H/4$ downstream (Fig. 6a).

Furthermore at XZ-plane, two main asymmetric recirculation zones behind the building are formed (Fig. 6a, $Y = 2$ m). The reattachment zone $L_{rec,b}$ (Table 1) behind the building extends up to around 14.6 m, smaller than in case A_1. As far as the XZ-plane flow inside the building is concerned, the air enters the inlet opening without changing the free-stream incidence angle, in contrast to the previously presented cases. At subsequent times, the air passes through the opening and hits the opposite leeward wall of the building, without being affected by the inner columns of the building. Consequently, one may note that in these cases more vortices – compared with cases A_1, A_2 and A_3 – are induced inside section A, from both sides of the entering air stream. Nevertheless, despite the complexity of the flow field inside the building, and especially at each room, the flow exits the building by having an almost perpendicular direction at the opening.

Regarding the normal planes inside the building, passing from the inlet and outlet openings centers, in the quarter-section D, a strong vortex is induced (Fig. 6b), which seems to alter as the Reynolds number increases, whilst on section A, not an easily distinguished recirculation area is spotted.

Outside the building and especially on the top of it, the air flow patterns seem to be unaffected by the different incidence angle. A small vortex is attached to the building's roof at its edge lying from the side of the outlet opening. Additionally, a big recirculation zone is induced in the whole area above the roof, especially in the plane passing normal to the outlet window (Table 1). The height of the aforementioned zone H_b (outlet window) is of almost the same size, compared to the respective one of the 0° incidence angle (Table 1).

The main reattachment zone $L_{rec,b}$ (Table 1) behind the building is asymmetric, due to the incidence angle of 30° and smaller than the corresponding one of the previous cases. Moreover, its length is decreasing as the Reynolds number increases.

As far as the local dimensionless pressure difference across the inlet and outlet windows, C_p, at their middle are concerned, the almost constant value of 0.68 for the incidence angle of 30° is

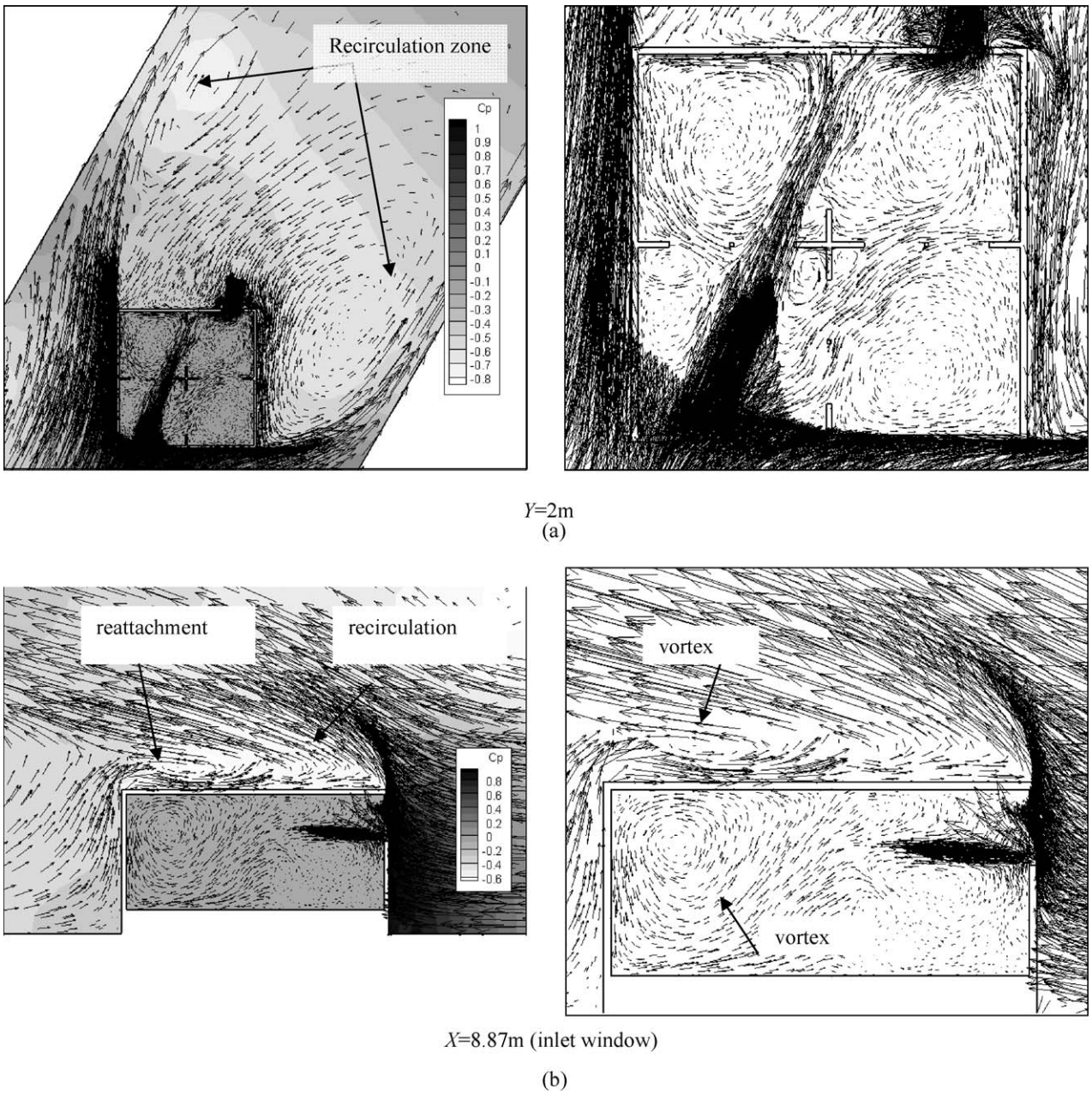

Fig. 6. (a) Induced pressure and velocity field for case B_2 at parallel plane $Y = 2$ m and (b) at normal plane $X = 8.87$ m (passing from the window's inlet center).

slightly smaller than the respective one for 0° (0.70), revealing that the inlet flow rate is slightly smaller at an incidence angle of 30° than at 0°, which is confirmed by both the corresponding experimental data and the present numerical results.

Fig. 7 presents the induced streamlines around the building in case B_1, coloured with the velocity's magnitude.

5.1.3. Incidence angle of 60°: cases C_1 ($U_\infty = 1$ m/s), C_2 ($U_\infty = 3$ m/s), C_3 ($U_\infty = 5$ m/s)

The cases described in this section are characterized by the same Reynolds number as in the previous sections, but by an incidence angle of 60°. The maximum pressure, which acts on the windward face of the building, is remaining almost the same as in cases B_1, B_2 and B_3 and equal to 100% of the initial total air inlet kinetic energy, as shown in Fig. 8a, at the plane laying in the middle of the openings height, $Y = 2$ m.

Regarding the induced velocity field around the building, the air travels attached and almost parallel to the right and left walls of the building, without creating a recirculation area on either side. On the other hand, one main recirculation zone is formed, which seems to begin from the left-side wall. It is worth noticing, that the reattachment zone reverses from the left side of the building moving towards the right one, inducing also a small recirculation just at the left leeward corner of the building. In conclusion, both the strength and dimensions of the entire air movement around the building remain unaffected by the wind speed (Table 2).

The reattachment zone behind the building $L_{rec,b}$ (Table 2) extends up to around 13.8 m, which is almost of the same size with the respective one at the incidence angle of 30° (case B_1). In addition, its dimensions are slightly decreasing, as the free-stream velocity increases.

At $Y = 2$ m, the air flow is entering the building from the inlet opening with almost the same incidence angle as the free-stream velocity of the wind. The main stream of the air seems to hit directly the right wall of the building and is driven with a direction normal to the outlet opening, following the flow direction of the

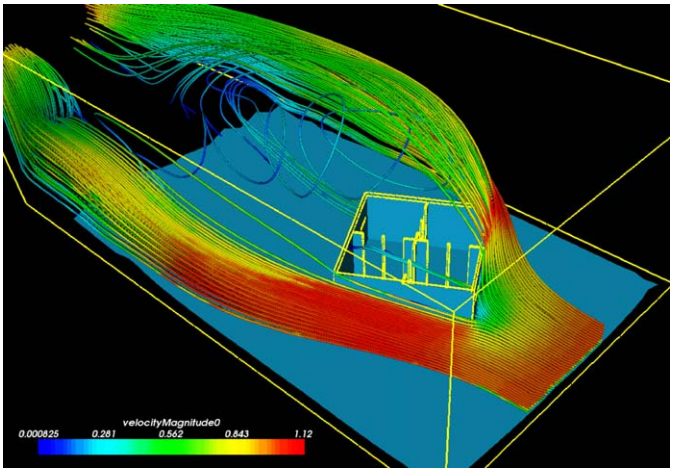

Fig. 7. Flow pathlines around the building for case B_1.

main recirculation area behind the building. The main path of the air inside the building generates five small recirculation areas distributed at the *XZ*-plane quarter-sections A–D.

As far as the normal planes, passing from the inlet window centers, are concerned, a reattachment of the flow to the buildings roof from the left side is evident. On the other hand, at the plane normal to the outlet window (Fig. 8b), a reattachment and a detachment zone are placed on the windward and leeward wall of the building, respectively. Moreover, the dimensions of the reattachment and detachment zones ($H_{f,s}$, $L_{f,s}$), which are present in these cases, seem to become slightly higher as the Reynolds number increases, in contrast to the ones previously presented (Table 2).

The local dimensionless pressure difference across the inlet and outlet openings, C_p, at their middle are equal to 0.19 and 0.06, respectively, which should have been ideally equal, if the pressure distribution did not vary so significantly on the area outside the outlet. Again, the non-dimensional character of the flow rate, passing through the inlet openings, and being independent of the Reynolds number is confirmed (Table 2). It is very important to

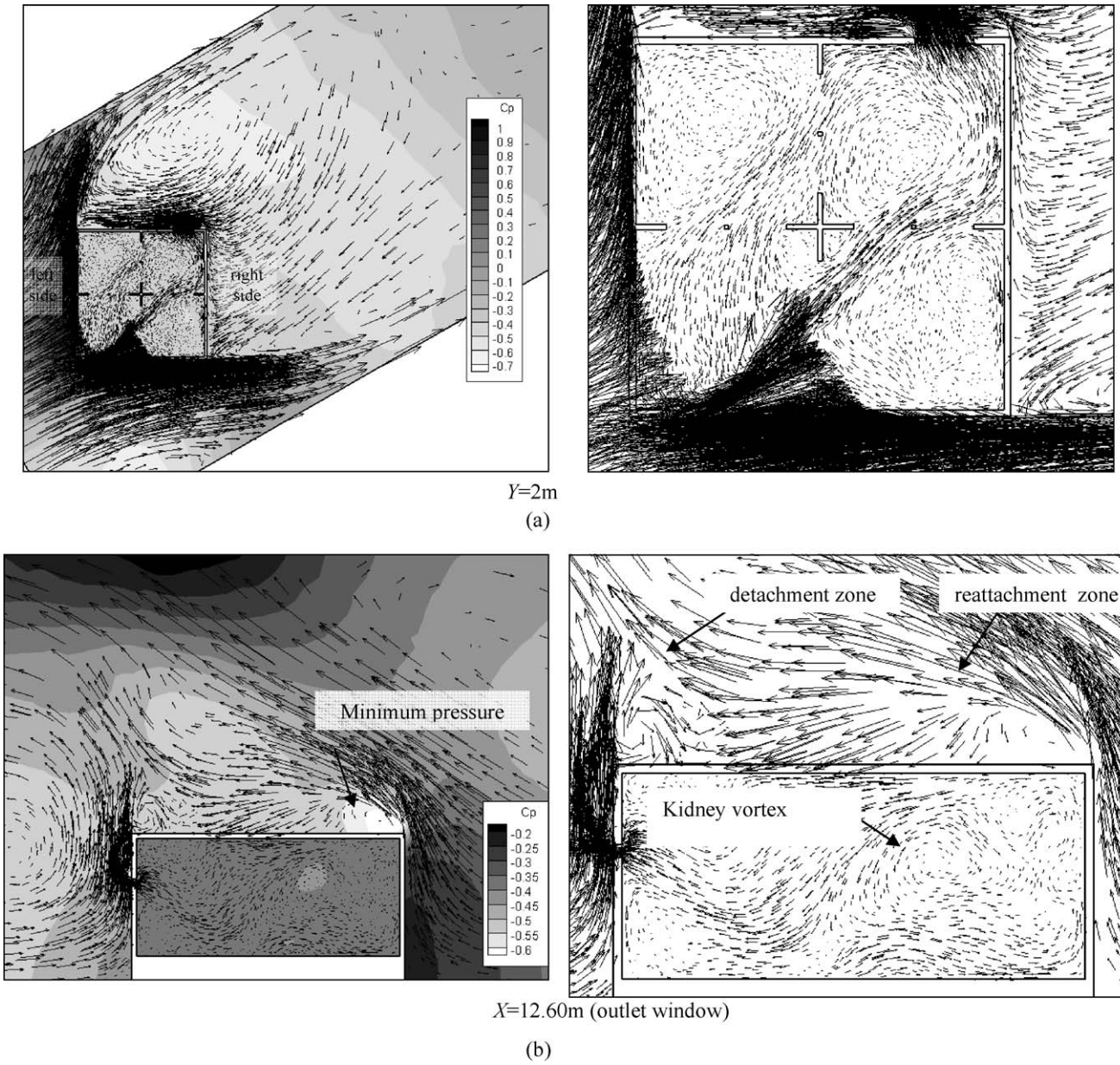

Fig. 8. (a) Induced pressure and velocity field for case C_3 at parallel plane $Y = 2$ m and (b) at normal plane $X = 12.60$ m (passing from the window's outlet center).

Table 2
Dimensions of induced flow field characteristics for cases C_1 to D_3.

Case	W_{bl}	W_{sl}	L_{sl}	W_{br}	W_{sr}	L_{sr}	H_s (inlet wind)/ (outlet wind)	L_{roof} (inlet wind)/ (outlet wind)	$H_{f,s}$ (inlet wind)/ (outlet wind)	$L_{f,s}$ (inlet wind)/ (outlet wind)	$L_{rec,f}$	$H_{rec,f}$	$L_{rec,b}$	$C_{p,max}$	C_p wind, inlet	C_p wind, out
C_1	6.15	–	–	–	–	–	0.51/0.75	0.64/0.59	–/0.74	–/1.14	0.78		13.8	100%	0.19	0.06
C_2	6.36	–	–	–	–	–	0.59/0.8	1.29/0.9	–/0.73	–/1.21	–	–	13.6	100%	0.19	0.08
C_3	6.36	–	–	–	–	–	0.4/0.91	1.39/0.93	–/0.75	–/1.21	–	–	13.2	100%	0.185	0.08
Case	W_{bl}	W_{sl}	L_{sl}	W_{br}	W_{sr}	L_{sr}	H_s (outlet wind)/ (inlet wind)	L_{roof} (outlet wind)/ (inlet wind)	$H_{f,s}$ (outlet wind)/ (inlet wind)	$L_{f,s}$ (outlet wind)/ (inlet wind)	$L_{rec,f}$	$H_{rec,f}$	$L_{rec,b}$	$C_{p,max}$	C_p wind, inlet	Cp wind, out
D_1	3.03	0.73	3.6	3.23	1.29	3.64	0.3/–	0.63/–	0.37/0.8	0.53/0.98	–	–	14.8	80%	0.033	0.018
D_2	2.91	1.03	3.97	3.39	1.23	3.6	0.46/–	0.78/–	0.37/0.79	0.92/0.70	–	–	14.3	80%	0.037	0.021
D_3	2.73	0.73	3	2.96	1.02	2.52	0.51/–	1.02/–	0.33/0.83	0.72/1.02	–	–	14.5	80%	0.035	0.022

notice that the value of C_p in these sub-cases is much lower than the respective previous ones, revealing that the flow rate inside the building is decreased for an incidence angle of 60° in contrast to 0° and 30°, which is confirmed by both the experimental data and the present numerical investigation.

5.1.4. Incidence angle of −90°: cases D_1 (U_∞ = 1 m/s), D_2 (U_∞ = 3 m/s), D_3 (U_∞ = 5 m/s)

The cases described in the following paragraph are characterized by the same wind free-stream velocities as in the previous ones, but by an incidence angle of −90°, which makes the building

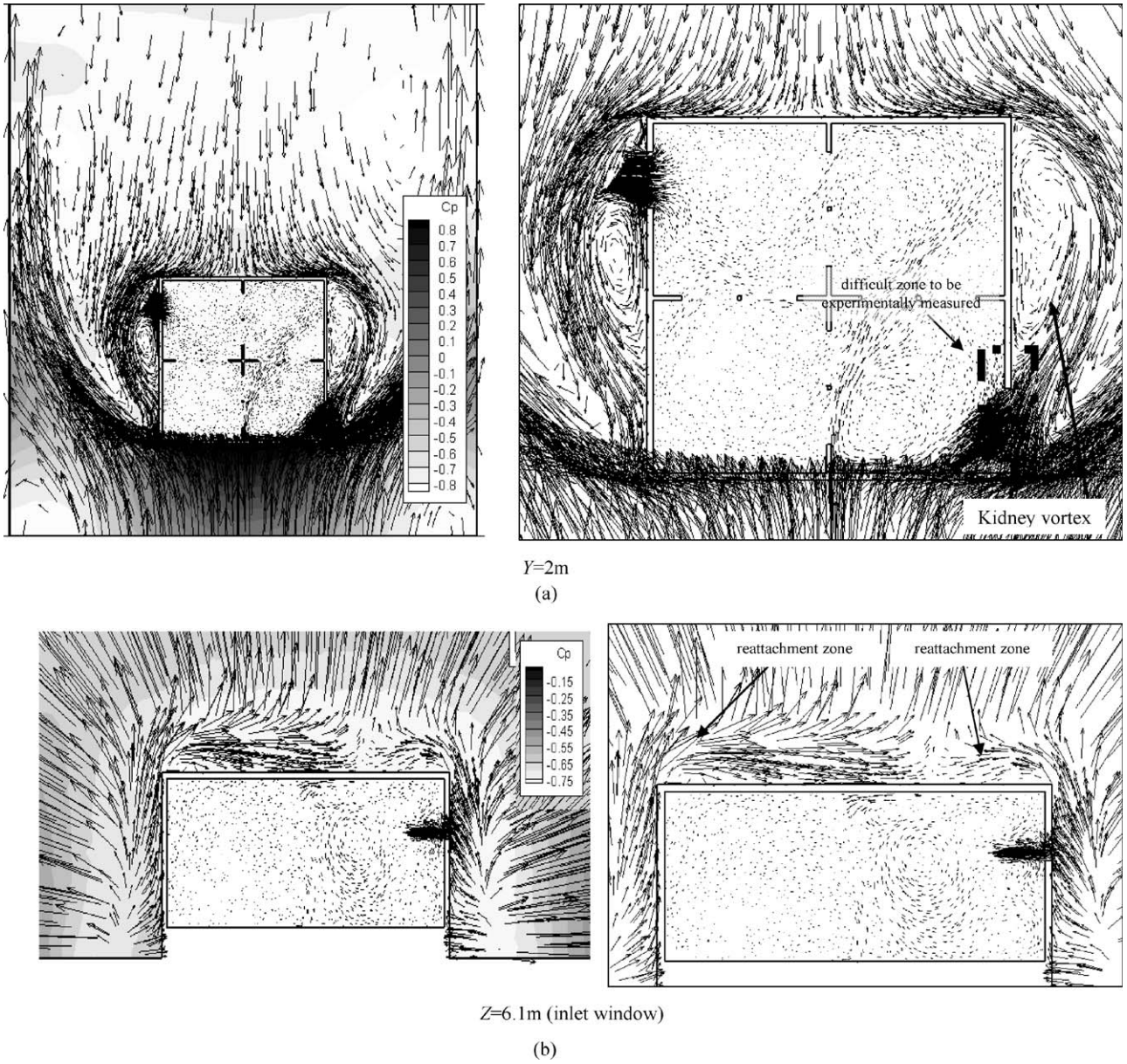

Fig. 9. (a) Induced pressure and velocity field for case D_2 at parallel plane Y = 2 m and (b) at normal plane Z = 6.1 m (passing from the window's outlet center).

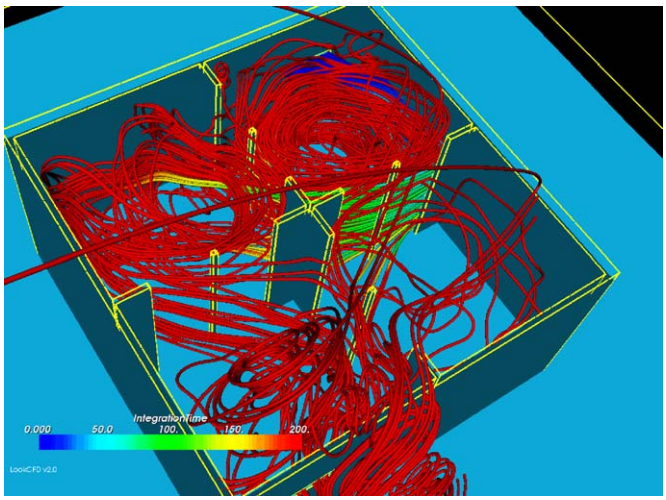

Fig. 10. Flow pathlines inside the building for case D_1.

stand in the same position as in cases A_1, A_2 and A_3, but changes the position of the openings, as shown in Fig. 9a. The same figure presents the pressure distribution and the induced velocity field and indicates that the maximum pressure values acting on the windward face of the building reach the same level of 80% of the initial total air inlet kinetic energy as in the cases of 0° incidence angle, assuring that these maximum values are not affected by the opening positions, but only by the incidence angle of the whole building.

Regarding the induced velocity field outside the building, the main wind flow hits on the windward side and generates two large symmetric recirculation zones, which are extended far downstream of the building and reattach the building side-walls. As a result of this reattachment, two other smaller recirculation zones of almost the same size (see Table 2) on the left and right sides of the building are formed (Fig. 9b), giving almost the same flow pattern as in the cases of 0° incidence angle. The right main recirculation has greater dimensions (W_{br}, L_{br}) than the left one (W_{bl}, L_{bl}), due to the fact that the embodied vortex, which is attached to the right side of the building, is characterized by a kidney vortex in contrast to the respective one to the left. Furthermore, the existence of the opening on the right side of the building drives the air to enter, thus increasing the vortex's length. However, its strength is lower compared with the corresponding one on the left-side, because the wind enters the building from the right and outflows from the left opening of the building, causing augmentation and reduction of the fluid momentum respectively. It should be mentioned, that in contrast to the previously presented cases, the air enters the opening, from which in all previously presented cases, the air outflows. This comes in total agreement with the corresponding experimental data by Larsen [26]. The overall flow field outside the building seems relatively unaffected by the higher values of free-stream velocity, as shown in Table 2, for cases D_2 and D_3, except for the dissipation of the kidney vortex formed on the right side of the building.

As far as the air flow inside the building is concerned, the wind enters the building from the right opening with an angle of around 40° hitting the front wall of the quarter-section A of the building, inducing a strong vortex inside it. On the contrary, the air flow is quite weak in the other sections, which makes difficult to locate other vortices formed, even in the cases of higher Reynolds number.

Regarding the normal planes, passing from the inlet window's center, two reattachment zones are induced on the left and right side of the building's roof (Fig. 9b, Z = 6.1 m), whose dimensions are not affected by the higher values of wind free-stream velocity of cases D_2 and D_3.

As far as the local dimensionless pressure difference across the inlet and outlet windows, C_p, at their middle are concerned, they are equal to around 0.035 and 0.018, respectively (Fig. 9a Z = 6.1 m, Z = 9.77 m, Table 2). It is very important to notice that the value of C_p in these sub-cases are the lowest among all cases, revealing that the flow rate inside the building is the smallest for an incidence angle of −90°, which is confirmed by both the experimental data and the present numerical investigation.

Fig. 10 presents the induced streamlines inside the building for case D_1, coloured with integration time of their calculation, respectively.

Table 3
Comparison between experimental and predicted values of aerating volume flow rates.

Incidence angle	U_∞ = 1 m/s	U_∞ = 3 m/s	U_∞ = 5 m/s
0			
Exprt. method (m^3/s) [26]	0.0698 (inlet) 0.0837 (outlet) 0.083 (decay)	0.218 (inlet) 0.244 (outlet) 0.241(decay)	0.345 (inlet) 0.394 (outlet) 0.352 (decay)
Present predictions (m^3/s)	0.0684 (k–ω model)	0.205 (k–ω model)	0.344 (k–ω model)
30			
Exprt. method (m^3/s) [26]	0.061 (inlet) 0.073 (outlet) 0.062 (decay)	0.198 (inlet) 0.220 (outlet) 0.186 (decay)	0.309 (inlet) 0.349 (outlet) 0.241 (decay)
Present predictions (m^3/s)	0.062 (k–ω model)	0.1879 (k–ω model)	0.31 (k–ω model)
60			
Exprt. method (m^3/s) [26]	0.027 (inlet) 0.030 (outlet) 0.028 (decay)	0.082 (inlet) 0.083 (outlet) 0.090 (decay)	0.134 (inlet) 0.144 (outlet) 0.145 (decay)
Present predictions (m^3/s)	0.0243 (k–ω model)	0.0625 (k–ω model)	0.12 (k–ω model)
−90			
Exprt. method (m^3/s) [26]	0.005 (inlet) 0.0079 (outlet) 0.014 (decay)	0.026 (inlet) 0.017 (outlet) 0.041 (decay)	0.029 (inlet) 0.044 (outlet) 0.062 (decay)
Present predictions (m^3/s)	0.0144 (k–ω model)	0.04 (k–ω model)	0.06 (k–ω model)

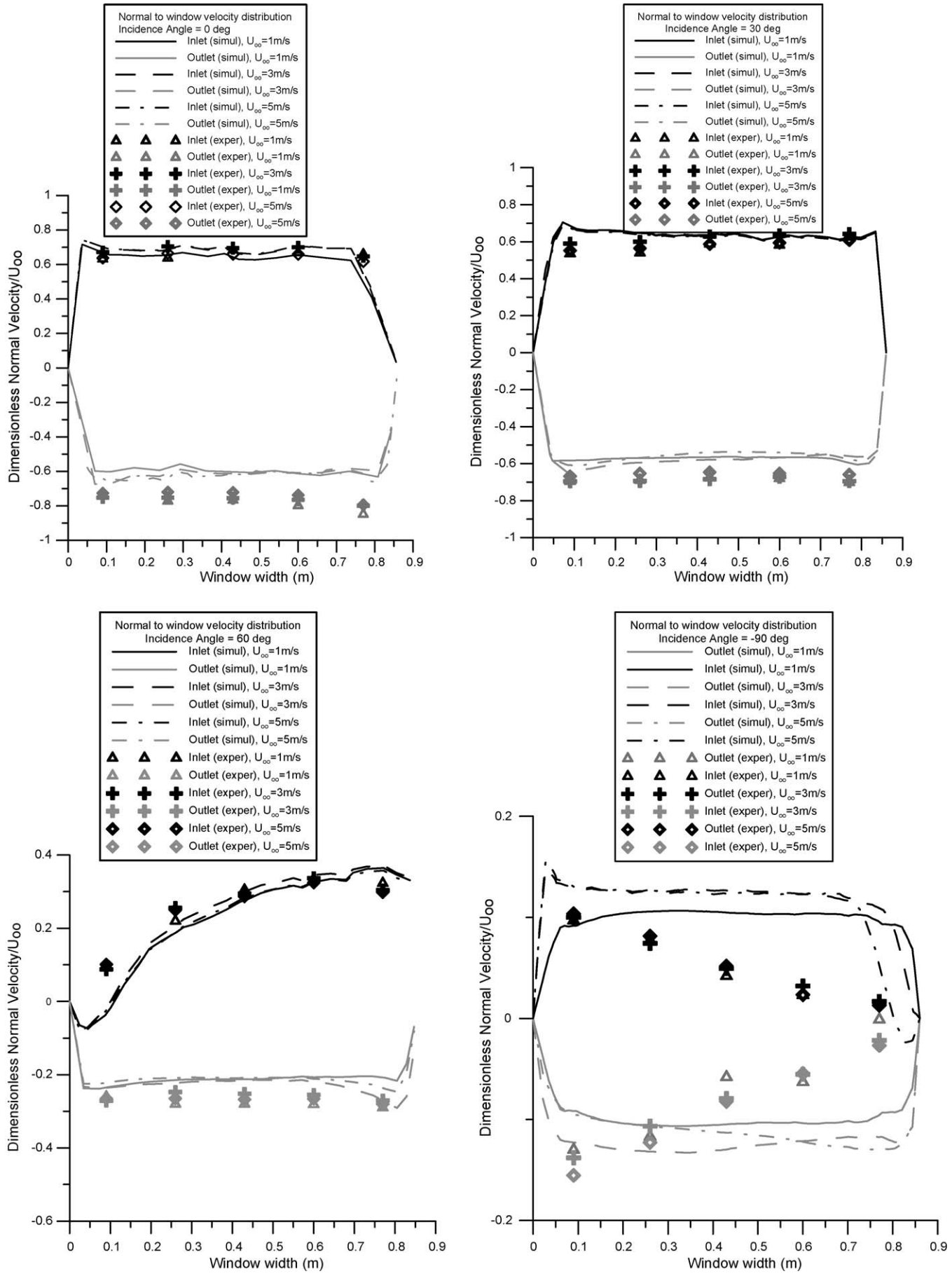

Fig. 11. Comparison of the numerical predicted dimensionless normal velocity distribution along the window's width with the corresponding experimental data for cases A_1 to D_3.

5.2. Air change rates in the building

In Table 3, the comparison between the numerical results with the corresponding experimental data (Larsen [26]), regarding the air volume flow rate aerating the building's room is presented. For each incidence angle and undisturbed wind free-stream velocity, U_∞, three different values of the measured volume flow rate, via different experimental methodologies, are given. The first two experimental methodologies are based on multiplying the measured velocities through inlet/outlet openings (windows) with the corresponding areas. The third one is based on the tracer gas measurements (decay method), assuming full mixing of tracer gas inside the building during the experiments, which is hard to get. From Table 3, it is evident that there are differences in the experimentally measured volume flow rates via the three methodologies. These deviations could be explained by the difficulties in deciding the right velocity profile near the edges of the opening, assumed to be – during the experiment – equal to zero at a distance of 2 cm away from the edge. This assumption aggravates, when the flow becomes very rough, especially in the case of the outlet opening methodology, where maximum differences between the experimentally measured volume flow rates are noticed (at the inlet and outlet openings is close to 45%), when, ideally, these flow rates should have been equal, as the numerical model predicts.

From Table 3, it is evident, that the air volume flow rate predicted by the numerical methodology does not agree in most of the cases with the corresponding experimental data obtained from the methodology based in the outlet opening. On the other hand, it agrees well with the corresponding experimental data obtained from the methodology based on the inlet opening, than with the tracer gas approximation for the cases of 0° and 30°. Better agreement of the flow rate with the first methodology is owed to the better agreement of the experimental and numerically predicted induced velocity profile at the inlet opening, than the outlet one (Fig. 11). For the case of an incidence angle of 60°, there is an under estimation of the numerically calculated volume flow rate in comparison with the experimental data (for all experimental methodologies), which may be attributed to the different velocity profiles obtained by the numerical results and the experimental data (Fig. 11), as explained in the next section.

Regarding the case of an incidence angle of −90°, the predicted volume flow rate agrees quite better with the decay experimental methodology than with the first methodology, because in that case the mixing of the tracer gas with the air is the best one among all cases, confirming that the tracer gas methodology works accurately, when the mixing is good, as also stated by Larsen [26].

5.3. Inlet and outlet velocity profiles

Fig. 11 presents the distribution of the dimensionless velocity component, normal to the opening window as a function of the window width. The numerical results agree quite well with the corresponding experimental data, especially for cases of an incidence angle of 0° and 30°, whilst differences exist for the case of 60°, especially moving towards the inlet opening left side (x = 0.1 m). In this zone, a reverse flow pattern is predicted, which is difficult to be measured by the hot wire methodology (capable of measuring the velocity magnitude only and not the direction). From Fig. 11, it is evident that this zone is not represented by the experimental data, revealing the difference in the aforementioned volume flow rate aerating the building, between the numerical results and the experimental data for this incidence angle.

For the case of −90°, although the predicted velocity profiles differ from the corresponding experimental ones measured with the first methodology, the predicted value agrees quite well with the flow rate measured with the tracer gas methodology. Furthermore, Fig. 11 reveals the non-dimensional character of the volume flow rate ventilating the building, both experimentally and numerically. This rate is almost proportional to the free-stream's velocity inlet.

5.4. Impact of building's inner topology on the air flow rate through openings

In order to check the effect of the inner building's topology on the ventilation rate of the building by natural means, the column behind the inlet window was subtracted and a new case is simulated with the same boundary conditions as in case A_1. Despite the fact that the predicted volume flow rate of inlet air did not change significantly, equal to 0.07 m^3/s, the flow pathlines of the air inside the building changed. It is shown that in case A_1 the fresh air travels inside the building for approximately 265 s passing mainly from sections A, B and C. In reference case A_1, section D is not highly aerated. On the contrary, for the geometrical configuration without the column, the air travels for about 150 s, passing through all the sections of the building, aerating most of its volume area, as shown in Fig. 12.

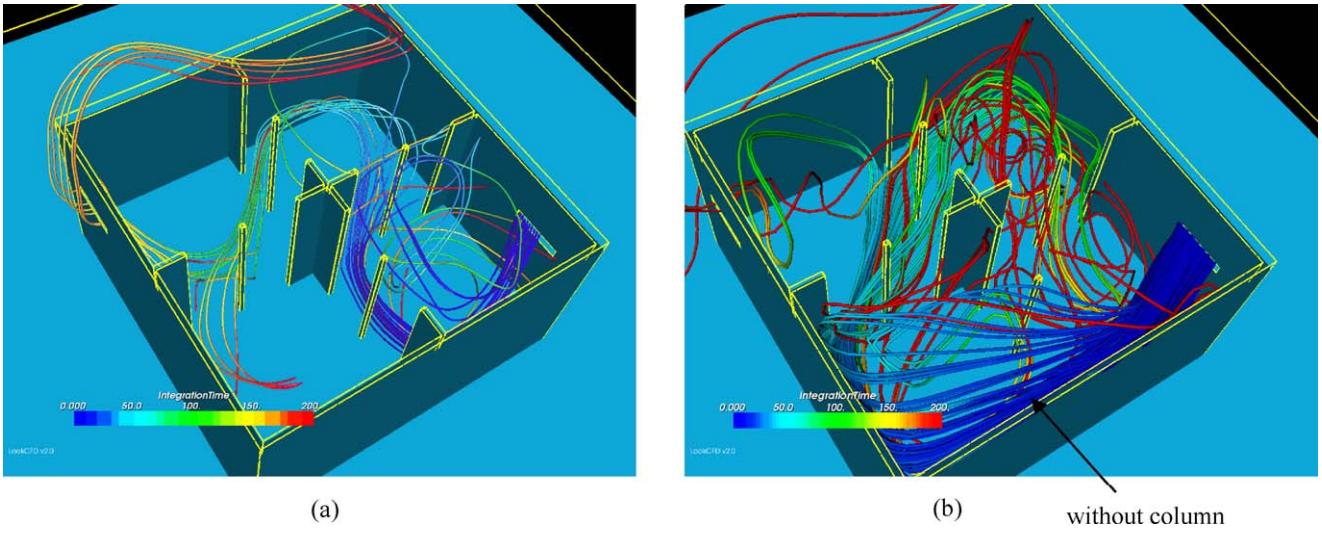

Fig. 12. (a) Flow paths of the air for case A_1 with and (b) without column.

6. Conclusions

The numerical predictions produced by CFD technique and especially using the k–ω turbulence model agree quite well with the corresponding available experimental data regarding the volume flow rate aerating the building and the induced velocity profiles, especially at the inlet window for a variety of incidence angles and free-stream's velocity profiles. Moreover, the numerical approach of such problems gives the opportunity for a better comprehension of the mechanisms of the natural ventilation in a building, by giving further insight on the induced flow field inside and around it with information, which could not be produced by experimental methods.

The present study confirms that, except for the geometry of the openings of a building and the incidence angle of the wind, the magnitude of the wind velocity plays an important role on the air-change rate of a building, due to its proportionality to the inlet volume flow rate. In addition, despite the fact that inner geometry of the building is not altering the aerating volume flow rate, it seems that it is a very important parameter for the refreshing rate of all the inner regions of building's envelope. Hence, in order to have a uniform ventilation of the building, the in depth study of its inner geometry is found to be really necessitated.

Finally, according to the numerical results, the first experimental methodology seems to be the most reliable than the two others. The tracer gas methodology depends on an a priory good and uniform mixing of the air with the relevant gas inside building, which is not always feasible, especially in the case of complex inside geometry as in our case (columns inside building) and high volume flow rates (cases A_1 to C_3), whilst the third methodology is based on a detailed and very accurate measurement of the complex induced velocity field (many and strong vortices) at the outlet window, which is much more difficult than the repective inlet one.

Acknowledgement

The authors would like to thank the lookcfd company (www.lookcfd.com) for the help they provided us in the representation of the induced flow field inside and outside the building via the corresponding figures.

References

[1] M. Orme, Estimates of the energy impact of ventilation and associated financial expenditures, Energy and Buildings 33 (2001) 199–205.
[2] C. Allocca, Q. Chen, L.R. Glicksman, Design analysis of single-sided natural ventilation, Energy and Buildings 35 (2003) 785–795.
[3] T. Katayama, J. Tsutsumi, A. Ishii, Full-scale measurements and wind tunnel tests on crossventilation, Journal of Wind Engineering and Industrial Aerodynamics 41–44 (1992) 2553–2562.
[4] E. Dascalaki, M. Santamouris, A. Argiriou, C. Helmis, D. Asimakopoulos, K. Papadopoulos, A. Soilemes, Predicting single sided natural ventilation rates in buildings, Solar Energy 55 (5) (1995) 327–341.
[5] J.E. Fernandez, B.J. Bailey, Measurement and prediction of greenhouse ventilation rates, Agricultural And Forest Meteorology 58 (3–4) (1992) 229–245.
[6] C.J. Koinakis, Combined thermal and natural ventilation modelling for long-term energy assessment: validation with experimental measurements, Energy and Buildings 37 (2005) 311–323.
[7] M.P. Straw, C.J. Baker, A.P. Robertson, Experimental measurements and computations of the wind-induced ventilation of a cubic structure, Journal of Wind Engineering and Industrial Aerodynamics 88 (2000) 213–230.
[8] W.A. Dagliesh, Comparison of model full-scale wind pressures on high-rise building, Journal of Industrial Aerodynamics 1 (1975) 55–66.
[9] R.L. Petersen, Wind tunnel investigation of the effect of platform-type structures on dispersion of eYuents from short stacks, Journal of Air Pollution Control Association 36 (1987) 1347–1352.
[10] M.M. Eftekhari, L.D. Marjanovic, D.J. Pinnock, Air flow distribution in and around a single-sided naturally ventilated room, Building and Environment 38 (2003) 389–397.
[11] N.H. Wong, S. Heryanto, The study of active stack effect to enhance natural ventilation using wind tunnel and computational fluid dynamics (CFD) simulations, Energy and Buildings 36 (2004) 668–678.
[12] L. Davidson, P. Nielsen, Large eddy simulation of the flow in a three-dimensional ventilation room, in: 5th International Conference on Air Distribution in Rooms, ROOMVENT96, July 17–19, 1996.
[13] W. Zhang, Q. Chen, Large eddy simulation of indoor airflow with a filtered dynamic subgrid scale model, International Journal of Heat Mass Transfer 43 (17) (2000) 3219–3231.
[14] W. Rodi, J.H. Ferziger, M. Breuer, M. Pourquié, Status of large eddy simulation: results of a workshop, Journal of Fluids Engineering 119 (1997) 248–262.
[15] S. Murakami, Overview of turbulence models applied in CWE-1997, Journal of Wind Engineering and Industrial Aerodynamics 74–76 (1998) 1–24.
[16] Y. Jiang, D. Alexander, H. Jenkins, R. Arthur, Q. Chen, Natural ventilation in buildings: measurements in a wind tunnel and numerical simulation with large-eddy simulation, Journal of Wind Engineering and Industrial Aerodynamics 91 (2003) 331–353.
[17] Y. Jiang, Q. Chen, Effect of fluctuating wind direction on cross natural ventilation in buildings from large eddy simulation, Building and Environment 37 (2002) 379–386.
[18] Y. Jiang, Q. Chen, Study of natural ventilation in buildings by large eddy simulation, Journal of Wind Engineering and Industrial Aerodynamics 89 (2001) 1155–1178.
[19] S. Murakami, Overview of turbulence models applied in CWE-1997, Journal of Wind Engineering and Industrial Aerodynamics 74–76 (1998).
[20] G. Iaccarino, P. Durbin, Unsteady 3D RANS simulations using the v2f model, Annual Research Briefs, Center for Turbulent Research (2000) 263–269.
[21] M.J. Cook, Y. Ji, G.R. Hunt, CFD modeling of natural ventilation: combined wind and buoyancy forces, International Journal of Ventilation 1 (3) (2003) 169–179.
[22] Q. Chen, Using computational tools to factor wind into architectural environment design, Energy in Buildings 36 (12) (2004) 1197–1209.
[23] S. Nishizawa, T. Savachi, K. Narita, H. Seto, Y. Ishikawa, A wind tunnel full scale building model comparison between experimental and CFD results based on the standard k–ε turbulence representation, International Journal of Ventilation 2 (4) (2003) 419–429.
[24] M.P. Straw, Computation and measurement of wind induced ventilation, PhD Thesis, School of Civil Engineering, University of Nottingham, 2000.
[25] G. Evola, V. Popov, Computational analysis of wind driven natural ventilation in buildings, Energy and Buildings 38 (2006) 491–501.
[26] T.S. Larsen, "Natural ventilation driven by wind and temperature difference", Ph.D. Thesis, Department of Civil Engineering, Group of Architectural Engineering, Aalborg University, 2005.
[27] T.S. Larsen, P. Heiselberg, Single-sided natural ventilation driven by wind pressure and temperature distribution, Energy and Buildings 40 (2008) 1031–1040.
[28] FLUENT 6.3 User's Guide, April 2009.
[29] B. Kader, Temperature and Concentration Profiles in Fully Turbulent Boundary Layers, International Journal of Heat Mass Transfer 24 (9) (1981) 1541–1544.